

---

This is an electronic reprint of the original article.  
This reprint may differ from the original in pagination and typographic detail.

Xu, Ying; Wu, Jiameng; Li, Pingshu; Kujala, Pentti; Hu, Zhiqiang; Chen, Gang  
**Investigation of the fracture mechanism of level ice with extended finite element method**

*Published in:*  
Ocean Engineering

*DOI:*  
[10.1016/j.oceaneng.2022.112048](https://doi.org/10.1016/j.oceaneng.2022.112048)

Published: 15/09/2022

*Document Version*  
Peer-reviewed accepted author manuscript, also known as Final accepted manuscript or Post-print

*Published under the following license:*  
CC BY-NC-ND

*Please cite the original version:*  
Xu, Y., Wu, J., Li, P., Kujala, P., Hu, Z., & Chen, G. (2022). Investigation of the fracture mechanism of level ice with extended finite element method. *Ocean Engineering*, 260, Article 112048.  
<https://doi.org/10.1016/j.oceaneng.2022.112048>

---

This material is protected by copyright and other intellectual property rights, and duplication or sale of all or part of any of the repository collections is not permitted, except that material may be duplicated by you for your research use or educational purposes in electronic or print form. You must obtain permission for any other use. Electronic or print copies may not be offered, whether for sale or otherwise to anyone who is not an authorised user.

Investigation of the fracture mechanism of level ice with extended finite element method  
Ying Xu <sup>a,b,\*</sup>, Jiameng Wu <sup>a,b</sup>, Pingshu Li <sup>a,b</sup>, Pentti Kujala <sup>c</sup>, Zhiqiang Hu <sup>d</sup>, Gang Chen <sup>a,b</sup>

<sup>a</sup> Marine Design and Research Institute of China, Shanghai, China

<sup>b</sup> Shanghai Key Laboratory of Ship Engineering, Shanghai, China

<sup>c</sup> Marine Technology, School of Engineering, Aalto University, P.O. Box 15300, 00076, Aalto, Finland

<sup>d</sup> School of Engineering, Newcastle University, Newcastle upon Tyne, NE1 7RU, UK

## Abstract

This paper investigates the fracture mechanism of level ice based on the extended finite element method by simulating collision scenarios between ice and a rigid ship structure. It is found the collision velocity and structure inclination affect the fracture mode through changing the deformation and stress distribution of the level ice. The overall response of the level ice is simulated with the transversely isotropic material model and cohesive zone model. The numerical model is verified with the data from a field test, which shows that the obtained ice load and size of the broken ices from numerical method are well consistent with the tested data. Two fracture modes of the level ice, bending and splitting, appear in the simulated cases. The bending crack is found to emerge from the top surface of the level ice and expand along the circumferential direction, and the splitting crack initiates at the bottom edge of the level ice and expands along the radial direction. Deformation and multiple stresses of level ice are analyzed, showing that the initial cracks for both fracture modes are related to the local tensile failure, and the location of the maximum tensile hydrostatic stress always coincides with the initial crack.

Keywords: ice load, level ice, fracture mechanism, splitting fracture, bending fracture

## 1. Introduction

Level ice is a type of sea ice commonly encountered by ships sailing in polar regions and might threat their safety. Therefore, calculating ice load on polar ships is an essential issue in ship resistance prediction and structural safety analysis. For the resistance prediction, the global ice load should be considered; while for structural safety analysis, local ice load is of more concern. It has been found that ice load is closely related to the complex breaking modes of level ice, and fracture is one of the major breaking modes that has been found to dominate the ice load (Riska, 2010). Different fracture modes such as bending and splitting, occur under different conditions and result in varying ice load characteristics. Therefore, to predict the ice load more accurately, it is essential to deeply investigate the mechanism of ice fracture.

In the prediction of ice load for level ice, empirical formulas are widely used in the initial stages of polar ship design and are acknowledged to be an effective method for engineering applications (Lindqvist, 1989; Keinonen et al., 1996; Riska et al., 1997). Lindqvist (1989) formula assumes that the level ice resistance on a ship is the sum of the resistance induced by level ice bending, crushing and submersion. This empirical formula constructs the relationship between parameters such as coefficients of ship hull, sea ice strength and thickness, as well as velocity. It affirms the importance of bending failure which is presented as circumferential fracture for the ice resistance. However, this method does not reflect the mechanism of sea ice fractures.

The current research on sea ice fracture mechanism is mainly achieved by analytical and semi-analytical methods. Many studies have focused on the analytical solution of fractures of level ice and ice floe. Kerr (1976) reviewed the analytical solutions of the floating ice plate with different loading and boundary conditions. Lu et al. (2015) investigated the out-of-plane failure of ice floe,

and previous studies on the failure patterns of ice floes with infinite size and semi-infinite size were also discussed in the work. Su et al., (2010) applied the analytical solutions that relates to ice wedge opening angle, ice strength and ice thickness to establish a numerical method to forecast the ice load continuously acting on the ship hull. This kind of approach solves many problems of ice fracture under specific loading ways and specific shapes of sea ice, however, it also has limitations due to complex sea ice conditions, such as strain rate effects and variable sea ice shapes.

Over the decades, the development of numerical methods has provided new ways for the calculation of ship-ice interaction. Common numerical methods for simulation of ice breaking include Finite Element Method (Gürtner, 2009; Liu et al., 2011; Xu et al., 2019), Discrete Element Method (Lilja et al., 2019; Liu and Ji, 2021; Ni et al., 2021), Peridynamics (Vazic et al., 2019; Xue et al., 2019), et al. Finite element method has been widely used to simulate ice breaking by removing solid elements or by separating two adherent elements, the latter also known as cohesive element method. Ehlers and Kujala (2014) used a plastic material model and element removing method in LS-DYNA to simulate the bending failure of ice beams. Sazidy (2015) simulated the bending fracture of ice wedge and the strain rate effect of the ice material is considered. Liu et al. (2011) and Xu et al. (2019) used finite element method and plastic ice material model to calculate ice load for iceberg impacts, in which the ice fracture is not simulated. Jeon and Kim (2021) combined plastic theory and damage mechanics to establish a material model for level ice, circumferential and splitting cracks of level ice interacting with a conical structure were simulated. Cohesive element method was applied by Gürtner (2009) in an early time to simulate the ice-structure interaction. The breaking process of level ice in interaction with columnar and inclined anti-ice arrangements were simulated. Lu et al. (2014) adopted cohesive element method to study the interaction of level ice and a conical structure, the bending failure of level ice was presented. Wang et al. (2019) used this method to study the continuous breaking process of level ice in ice-ship interaction and bending fractures were simulated successfully. Recent studies using cohesive element method to study sea ice can also refer to Zhou et al. (2019), Patil et al. (2021) and Kellner et al. (2021). Compared with traditional finite element method, cohesive element method can better simulate the ice fracture. However, in cohesive element method, the crack extends along the edges of the elements, so the crack propagation is restricted by the mesh division. This method has other mesh-dependent drawbacks, which have been discussed in Lu et al. (2014) and Wang et al. (2019).

Extended finite element method is based on traditional finite element method, introducing enrichment functions into the displacement approximation function to increase the freedom degrees to describe discontinuous deformation, so that the crack can pass through the interior of element. In this way, the extended finite element method is less dependent on mesh and can present a more graphic fracture phenomenon. Lu et al. (2012) firstly applied extended finite element method to simulate the failure of ice wedge, and the results showed that the bending fracture could be well presented by this method. After that, Lu et al. (2017; 2018) established a numerical scheme for simulating splitting cracks of ice floe and investigated the fracture mechanism of sea ice between parallel channels. The feasibility of using this approach to study splitting cracking was verified by comparing the numerical results with full-scale ship tests and ice floe fracture tests. Li et al. (2020) used extended finite element method to calculate the bending load of level ice and built a tool for ship-ice interaction calculation accordingly. Xu et al. (2020) proposed a numerical scheme based on the extended finite element method to simulate the interaction of level ice and landing craft bow, and to study the fracture mode and ice load of level ice. The simulated ice load and fracture ice size were in good agreement with the field test results.

The above studies demonstrate the effectiveness of the extended finite element method for sea

ice fracture simulation. However, previous studies still lack the investigation of sea ice fracture mechanism. This paper aims to study the initiation and expansion process of splitting and bending fractures in level ice, and to investigate the internal mechanism and influencing factors that trigger different fracture modes. This is achieved by simulating the collision between level ice and a flat structure based on extended finite element method. The flat structure can be considered as a simplified local structure of a ship.

In the investigation of mechanical mechanism that triggers the fracture of level ice, the level ice deformation and multiple stresses are demonstrated and analyzed. Considering the mechanical characteristics of sea ice are closer to materials such as rocks and concretes, the maximum principal stress and hydrostatic stress instead of Von Mises stress are discussed. In addition, the components in the level ice stress tensor are displayed. Whether and how these stresses are related to the fracture of ice will be analyzed in this paper.

In the following content, Section 2 introduces the basic theory of extended finite element method. Section 3 establishes the numerical model, including the adopted sea ice material model, fracture criterion and model mesh. Section 4 displays and analyzes the simulation results. Ice load on the structure and size of the broken ice are compared with the data from field tests to verify the accuracy of the method. The simulated results of the bending fracture and splitting fracture are discussed separately, including the continuous deformation of the ice, the crack initiation and crack propagation process, as well as the stress distribution of the level ice. Then the influence of the collision velocity and structure inclination angle on the level ice fracture are discussed. Level ice deformation and multiple stresses distribution in different collision conditions will be compared and analyzed to explore the mechanism of ice fracture. The research outcomes of this study will benefit the shipbuilding industry to achieve better understanding of ship-ice interaction and analysis tool for numerical simulations.

## 2. Theory

### 2.1 Basic theory of extended finite element method

The extended finite element method is based on the traditional finite element approach and unit decomposition, introduces enrichment functions in the approximation function to increase the degrees of freedom for describing discontinuous deformations, so that the crack can pass through the interior of the cell without constantly updating the mesh. The virtual node method is usually used to generate nodes at the crack face and the geometry of the crack is described using the level set method, and linear elastic fracture mechanics or cohesive model is applied to describe the intrinsic relationship of the crack.

$$\mathbf{u} = \sum_{i \in I} N_i \mathbf{u}_i + \sum_{j \in J} N_j H(f(x)) \mathbf{a}_j + \sum_{k \in K} N_k \left( \sum_{l=1}^L F_l(x) \mathbf{b}_k^l \right) \quad (1)$$

where  $J$  represents all nodes that the corresponding shape functions are completely cleaved, and the corresponding node' enriched degrees of freedom is  $\mathbf{a}_j$ ,  $H(f(x))$  is the continuous step function of the crack surface;  $K$  represents all nodes of the cell containing the crack tip, and the corresponding node-enriched degrees of freedom is  $\mathbf{b}_k^l$ ,  $F_l(x)$  is the crack tip approximation function.

### 2.2 Cohesive model and its application in extended finite element method

The cohesive model assumes a fracture process zone, where micro-cracks and damages exist at the crack tip area. To account for this, the cohesive model extends the actual macroscopic crack by a segment forward, which is a virtual crack (Dempsey et al., 2018). A stress-displacement curve can be used to describe the crack formation and opening process, as shown in Figure 1.

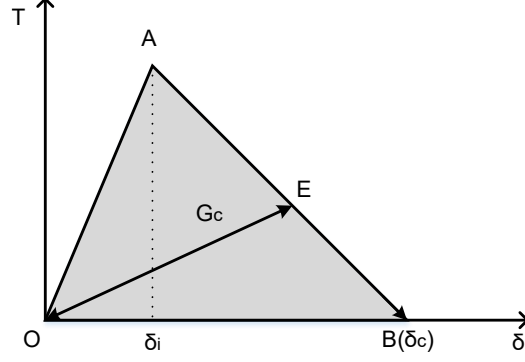


Figure 1. Stress-displacement curve for the crack

The stress-displacement relationship of the cohesive model includes two phases: the linear stress development phase and the damage accumulation phase, represented as OA and AB. And the simulation of damage includes two criteria: the damage initial criterion and the damage accumulation criterion. Before reaching the damage initial criterion, the stress develops according to the linear elastic law, while after reaching the damage initial criterion, the damage accumulates according to a defined law. In the extended finite element, the stress softening is achieved by changing the stiffness matrix.

(1) Linear stress development phase

The stress-displacement model in the linear elastic phase can be expressed as a relation between the stress matrix and displacement matrix connected by the stiffness matrix  $K$ ,

$$\begin{Bmatrix} T_n \\ T_s \\ T_t \end{Bmatrix} = \begin{bmatrix} K_n & 0 & 0 \\ 0 & K_s & 0 \\ 0 & 0 & K_t \end{bmatrix} \begin{Bmatrix} \delta_n \\ \delta_s \\ \delta_t \end{Bmatrix} \quad (2)$$

where  $T_n$ ,  $T_s$  and  $T_t$  are the normal tensile stresses and shear tensile stresses.  $\delta_n$ ,  $\delta_s$  and  $\delta_t$  are the normal separated displacement and shear separated displacements.  $K_n$ ,  $K_s$ , and  $K_t$  are the components of the cohesive stiffness matrix which is determined by the material model of the ice element.

(2) Damage accumulation phase

In the damage accumulation phase, the stress-displacement relationship is described by the softening of the cohesive stiffness  $K$ , then the relationship could be written as,

$$\begin{aligned} t_n &= \begin{cases} (1-D)T_n, & T_n \geq 0 \\ T_n, & T_n < 0 \end{cases} \\ t_s &= (1-D)T_s \\ t_t &= (1-D)T_t \end{aligned} \quad (3)$$

where  $t_n$ ,  $t_s$  and  $t_t$  are the normal tensile stresses and two shear stresses in the damage phase, respectively.  $D$  is the damage variable with an initial value of 0 and an upper limit of 1.  $D=0$  (point A) represents no damage, and  $D=1$  (point B) represents the full development of damage and tensile force between the crack surfaces disappears. When the normal stress is compressive stress, no damage occurs.

If the displacement decreases in this phase, the stress will degrade along EO. And if the displacement increases again, the stress will develop along OEB if the displacement increases again. The area enclosed by OAB is the fracture energy  $G_c$ . Since the cohesive stiffness  $K$  in the elastic phase is calculated from the material model of the ice bulk element, the complete stress-

displacement curve can be calculated by specifying the damage accumulation law and the fracture energy  $G_C$ . In this paper, a linear damage accumulation law is adopted.

### 3. Numerical model

#### 3.1 Extended finite element model

This paper simulated the level ice collision scenario based on the field test conducting in the Baltic Sea off the west coast of Finland. The level ice was collided with a landing craft bow, which was a flat-shaped structure installed at the front of a ship. More information of the field test could be found in Varsta (1983). The shape of the level ice cracks, the ice load and the size of the broken ice under different collision speeds and bow inclination angles were recorded. Thus the numerical model can be verified through comparing the simulated results with the above information.

Based on the field test situations, the level ice model is established as a flat plate of finite size, and the landing craft bow is simplified as a rigid plate, as shown in Figure 2. The size of the modeled level ice is 180m\*90m\*0.36m to ensure that the ice is large enough to avoid interference from boundary conditions on the simulation results. Three edges of the level ice are fixed, and the edge going to contact with the rigid plate is free. An ice wedge is trimmed according to the field test and this area will collide with the landing craft bow, as shown in Figure 3.

The landing craft bow is established as a rigid plate. The ship hull of the tug is not available, so it is not built in the simulation, and its movement in directions other than the forward direction is intentionally omitted. Constant velocity along x direction is applied to the rigid plate, and it's fixed in other directions. The buoyancy of water is simulated with uniformly arranged springs at the bottom of the level ice, and the added masses are not taken into account for neither ice nor ship. Six cases of different collision velocities and inclination angles are simulated. The numerical simulations are completed in ABAQUS, and the relevant parameters of simulated cases are illustrated in Table 1 and Table 2.

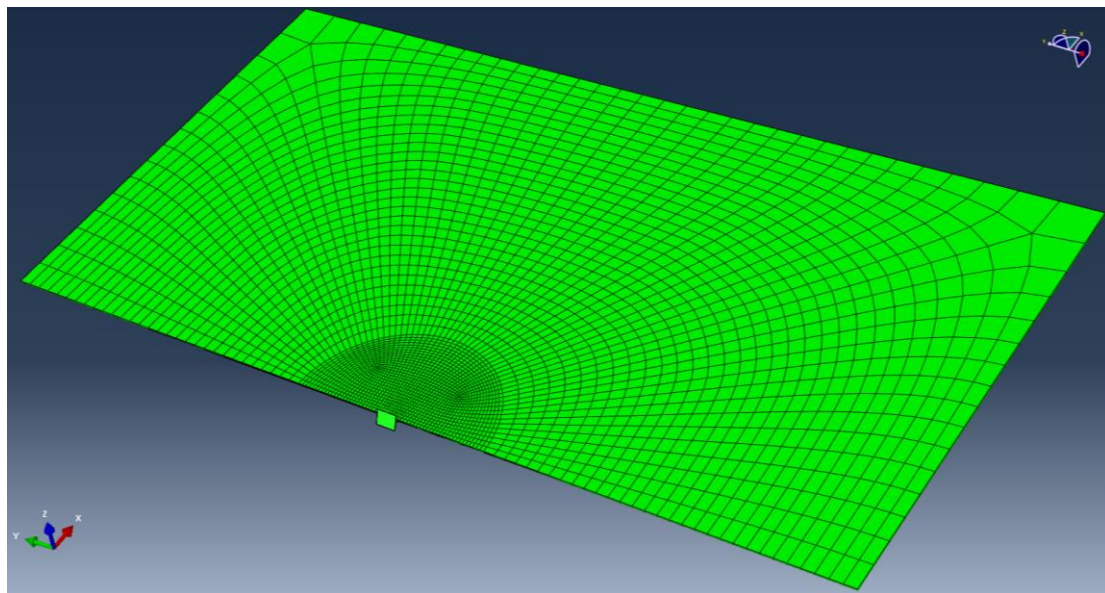


Figure 2. Finite element model of the landing craft bow impact on level ice

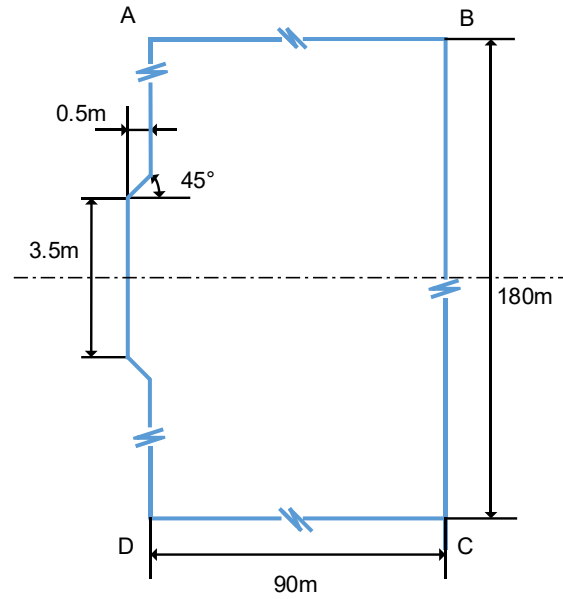


Figure 3. Geometry and size of the level ice model

Table 1. Parameters of the rigid plate

Item	Unit	Value
Length	m	5
Width	m	2.5
Inclination angle	deg	30, 50
Velocity	m/s	1.2, 2, 3

Table 2. Parameters of the level ice and water

Item	Unit	Value
Thickness of ice	m	0.36
Density of ice	kg/m <sup>3</sup>	900
Density of water	kg/m <sup>3</sup>	1025
Friction coefficient between ice and plate	-	0.1
Fracture energy	N/m	5

### 3.2 Ice bulk material model

The level ice simulated in this paper is columnar grain ice that the long axis of the ice grain is aligned with the vertical direction. Thus the mechanical properties of level ice are isotropic in the horizontal plane, and the mechanical properties in the horizontal direction are different from those in the vertical direction. Therefore, a transversely isotropic material model is used to simulate the level ice, and it is assumed that the randomness caused by micro-cracks and impurities is not considered.

For the transversely isotropic stress-strain relationship, five independent constants can be used to construct the stiffness matrix,

$$\begin{bmatrix} \Delta \varepsilon_1 \\ \Delta \varepsilon_2 \\ \Delta \varepsilon_3 \\ \Delta \gamma_{23} \\ \Delta \gamma_{31} \\ \Delta \gamma_{12} \end{bmatrix} = \begin{bmatrix} 1/E_1 & -\nu_{11}/E_1 & -\nu_{31}/E_3 & & & \\ -\nu_{11}/E_1 & 1/E_1 & -\nu_{31}/E_3 & & & \\ -\nu_{31}/E_3 & -\nu_{31}/E_3 & 1/E_3 & & & \\ & & & 1/G_{31} & & \\ & & & & 1/G_{31} & \\ & & & & & 2(1+\nu_{11})/E_1 \end{bmatrix} \begin{bmatrix} \Delta \sigma_1 \\ \Delta \sigma_2 \\ \Delta \sigma_3 \\ \Delta \tau_{23} \\ \Delta \tau_{31} \\ \Delta \tau_{12} \end{bmatrix} \quad (4)$$

where  $\Delta \varepsilon$  and  $\Delta \sigma$  are the normal strain and stress,  $\Delta \gamma$  and  $\Delta \tau$  are the shear strain and stress,  $E_1$  is the elastic modulus parallel to the isotropic plane,  $E_2$  is the elastic modulus perpendicular to the isotropic plane,  $G_{31}$  is the shear modulus perpendicular to the isotropic plane,  $\nu_{11}$  is the Poisson's ratio in the isotropic plane,  $\nu_{31}$  is the Poisson's ratio perpendicular to the isotropic plane. The values of the relevant material parameters are shown in Table 3, and the data source is referred to Varsta (1983).

Table 3. Elastic constants of the ice material model.

Elastic constant	$E_1$	$E_3$	$\nu_{11}$	$\nu_{31}$	$G_{31}$
Unit	GPa	GPa	-	-	GPa
Value	7.28	10.16	0.59	0.34	2.48

### 3.3 Crack initiation and propagation criterion

It is assumed that when the stress of the level ice reaches a certain state, initial crack occurs at the corresponding location. A transversely isotropic failure criterion is adopted,

$$f(\sigma) = F_{11}(\sigma_1 + \sigma_2) + F_{33}\sigma_3 + G_{1111}(\sigma_1^2 + \sigma_2^2) + G_{3333}\sigma_3^2 + 2G_{1122}\sigma_1\sigma_2 + 2G_{1133}(\sigma_1 + \sigma_2)\sigma_3 + 4G_{1313}(\sigma_1^2 + \sigma_2^2) + 4G_{1212}\sigma_6^2 \quad (5)$$

where  $F_{ij}$  and  $G_{ij}$  are mechanical constants that can be obtained from ice strength tests. The adopted values of the parameters are shown in Table 4, and the parameter evaluation process could be referred to Varsta (1983).  $f(\sigma)=1$  is the failure surface. When  $f(\sigma)<1$ , the level ice does not crack. When  $f(\sigma)\geq 1$ , the failure criterion is satisfied and the crack initiates. The crack propagation law obeys to the stress-displacement criterion in Section 2.2.

Table 4. Mechanical parameters in Tsai-Wu failure criterion.

Parameter	Unit	Value
$F_{11}$	MPa <sup>-1</sup>	1.550
$F_{33}$	MPa <sup>-1</sup>	0.806
$G_{1111}$	MPa <sup>-1</sup>	0.491
$G_{3333}$	MPa <sup>-2</sup>	0.194
$G_{1122}$	MPa <sup>-2</sup>	-0.395
$G_{1133}$	MPa <sup>-2</sup>	0.062
$G_{1313}$	MPa <sup>-2</sup>	0.345

### 3.4 Contact and mesh parameters

One-order reduced solid elements are used in level ice to perform the extended finite element analysis, and shell element is used for the rigid plate. The implicit time integration algorithm is used for the calculation in ABAQUS. According to the experimental phenomena, the areas where cracks may appear are all around the wedge-shaped part of the level ice. Therefore, the enrichment property is assigned to the area with a radius of 4 m centered in the middle of the contact edge, so that the crack could emerge and develop in this area. A narrow area along the contact edge undergoes crush failure rather than fractures that bend or split the level ice. Therefore, it is assumed that the fracture does not initiate in this region, and the “over-closure contact algorithm” is applied to deal with the crush forces. The contact pressure-penetration depth relation is defined according to the results of crushing experiment on ice wedge in Varsta (1983). The friction coefficient between ice and the rigid plate is assumed to be 0.1.

The assumption that crack not initiates from the contact area is made based on the following reasons. First, according to the data analysis of the field test, there is no description about cracks propagating from the contact area that would cause the level ice breaking overall. Ice in the contact area mainly undergoes local crushing failure. Second, XFEM in ABAQUS can't handle crack intersection and bifurcation, which means if the small cracks in local crushing tend to intersect, it will lead to incorrect results. Therefore, it is assumed that the cracks are not allowed to emerge from the contact zone to simplify the treatment of the ice crushing phenomenon, and instead a contact algorithm is used to guarantee the crushing force as realistic as possible to obtain a plausible results of the overall fracture of the level ice.

In the contact area and the area where fractures tend to appear, the model is meshed more densely. The further away from the contact zone the sparser the grid is. And in the thickness direction, on purpose of simulating the crack propagation path accurately, the level ice model should be divided into as many elements as possible. After several attempts and consider the computation efficiency, seven layers of elements were divided along the thickness direction.

The effect of mesh size in horizontal direction of the ice plate is studied in detail. The mesh size in the area where cracks may exist is of interest especially. The mesh sizes of the ice discussed in this work are 1m\*0.6m, 0.67m\*0.45m, 0.4m\*0.45m, 0.2m\*0.2m. The authors combined the calculation cost, the size of the ship-ice contact area, and the size of the fractures, then the mesh sizes are chosen after several attempts. The aspect ratio of the mesh is not discussed intentionally, but the mesh shapes are supposed to be regular, thus the aspect ratio is not larger than 2. The ice load and size of the broken ice under different mesh sizes are summarized in Table 5. Compared to the model size of the enriched region, the mesh size of 1m\*0.6m is very coarse, and 0.2m\*0.2m is defined as very fine. As the grid size decreases, ice load also decreases. For 0.4m\*0.45m and 0.2m\*0.2m, the simulated ice loads are very close, showing that the decrease trend is weakening. The size of the broken ice is very stable as the mesh varies. In the simulation, the very fine mesh is used to ensure the crack developing process and stresses distribution can be well captured.

Table 5. Mesh sensitivity analysis results

Mesh size (m)	Ice load (MN)	Size of the broken ice (m)
1*0.6	0.728	2.2
0.67*0.45	0.557	2.17
0.4*0.45	0.524	2.3

---

## 4. Results and discussions

According to the simulated results, bending fracture emerges in five cases, splitting fracture emerges in two cases, and both bending and splitting fracture emerge in one of these cases. This section will discuss the development process of bending fracture and splitting fracture respectively, and analyze the deformation and stress distribution of the level ice. Then the results of all the cases with different collision velocities and inclination angles of the rigid plate will be compared to investigate the ice fracture mechanical properties. The numerical model has been verified first, and the verification is placed in Section 4.3 to discuss with the influencing factors together.

### 4.1 Bending fracture

#### 4.1.1 Bending fracture initiation and propagation

Bending crack emerges in most of the simulated cases. This part uses  $\beta=50^\circ$ ,  $v=2\text{m/s}$  case as an example to discuss the bending crack mechanism. Figure 4 illustrates the crack initiating and propagating with time.

In the numerical simulation, the variation of  $f$ -value in equation (5) can represent the process from no crack to crack initiation. At  $t=2\text{ms}$ , the maximum  $f$ -value is 0.2177, and the corresponding point is at one waist of the ice wedge. At the same time, another point at the top surface midline also reached a relative high  $f$ -value. At  $t=4\text{ms}$ , the maximum  $f$ -value area shifts to the top surface midline. The  $f$ -value decreases along the center around midline towards the periphery at this moment, showing a growth ring-like distribution. As the collision proceeds, the high  $f$ -value area gets farther away from the contact area along the  $x$  direction, and the  $f$ -value keeps increasing. At  $t=7\text{ms}$ , the maximum  $f$ -value increases to 1, and the initial crack emerges where  $x=1.81\text{m}$ . Then the crack propagates along an arc route, and it takes 5.2ms for the crack from initiating to penetrating the top surface of the level ice.

Theoretically XFEM is enabled to keep the crack tip inside the cell, but ABAQUS doesn't allow this. The crack will only extend if it reaches the point where the crack can cross the cell and stop on the cell boundary, thus reducing the complexity of the calculation. This is also stated in the ABAQUS Analysis User's Guide (2019). For this limitation, the simulated results shown in Figure 4 have the crack tips resting on the cell boundaries.

Overall, the bending fracture in the simulation initiates from the top surface of the ice and propagates to be an arc-shaped crack. The bending fracture matches well in morphology with the fracture obtained in the field test, which is illustrated in Figure 5. It should be noted that one point at the bottom of the ice also reached a relative high  $f$ -value. But it's only 0.4 at  $t=0.7\text{ms}$ , and never comes to 1 in the entire simulation, so no crack will emerge at the bottom in this case.

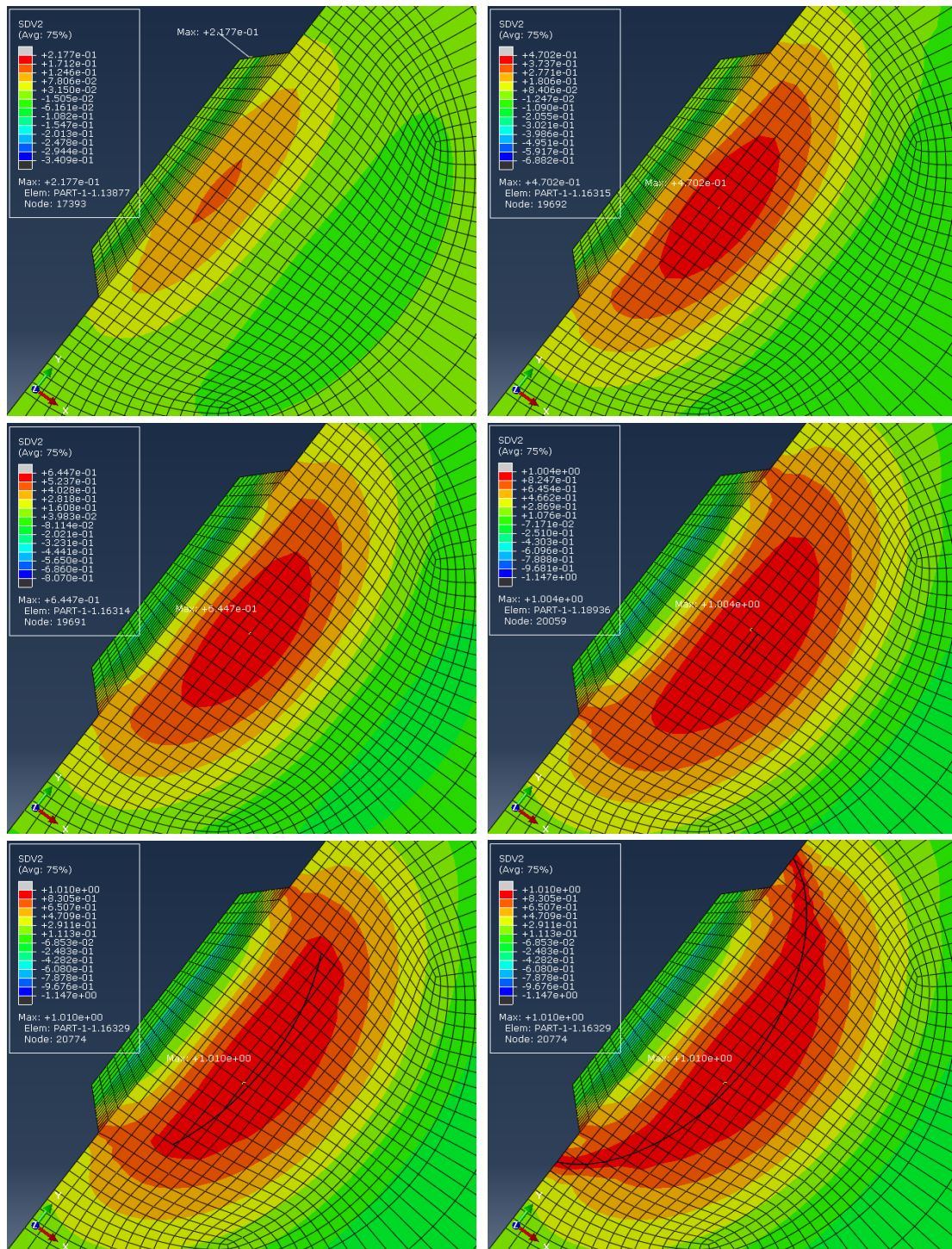


Figure 4. Distribution of crack initiation function  $f$  at the top surface of the level ice. Time  $t=2\text{ms}$ ,  $4\text{ms}$ ,  $5\text{ms}$ ,  $7\text{ms}$ ,  $8\text{ms}$ ,  $12.2\text{ms}$  from contacting with the rigid plate in the case of  $\beta=50^\circ$ ,  $v=2\text{m/s}$

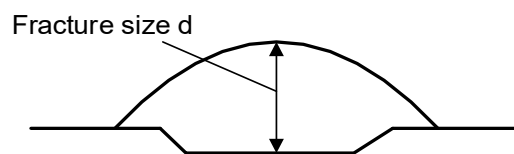


Figure 5. The bending crack recorded in the field test.

#### 4.1.2 Ice load and ice deformation

(1) Ice load developing in time series

Ice load develops along with the ice-structure contact and interact with each other. In the simulation, it is assumed that the contact force increases with the contact area increasing. Figure 6 (left) shows the ice load developing in time series and labels the ice load corresponding to the crack initiation. It takes 7ms from collision onset to crack initiation, and 5.2ms from crack initiation to crack penetration of the top surface of level ice. The crack develops very quickly and needs to be timed in milliseconds. According to the simulation results, the ice load continues to increase with time and shows a certain curvature. In the compression between the structure and the level ice, the level ice bends downward which affects the shape of the contact area. In this case, the ice load at the crack initiation time is 0.149MN, and ice load at crack penetration time is 0.238MN.

Figure 6 (right) illustrates the total contact force between the ice and the structure, including the crushing force and the friction force. The friction force in this case is 0.0238MN at  $t=12.2\text{ms}$  and is upward along the contact surface. The total force can be divided into another two components, along  $x$  direction and opposite to  $z$  direction respectively. The vertical component makes the ice bend downwards, and the horizontal component causes the ice to produce in-plane extrusion.

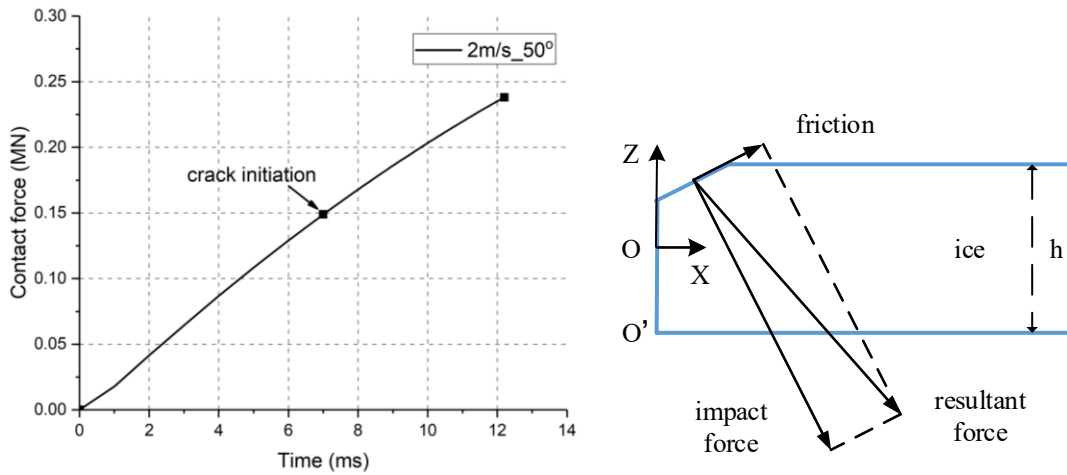


Figure 6. Simulated ice load-time curve ( $\beta=50^\circ$ ,  $v=2\text{m/s}$ ) (left) and schematic of contact force on ice (right)

(2) Ice deformation

The simulated level ice deformation process includes three stages: continuous deformation, crack initiation, crack propagation. In Figure 7,  $U1/U2/U3$  represent the deformation of level ice in  $x/y/z$  direction respectively at the crack initiation time. The  $U3$  displacement shows that the ice moves downwards along  $z$  axis, representing the bending deformation of the level ice. The  $U1$  value on the top surface and the bottom surface of the ice is negative and positive respectively, indicating the top surface is stretching and the bottom surface is compressing. And the distribution of  $U2$  shows that the wedge corners on the top surface move towards each other, and the bottom wedge corners move in opposite directions.

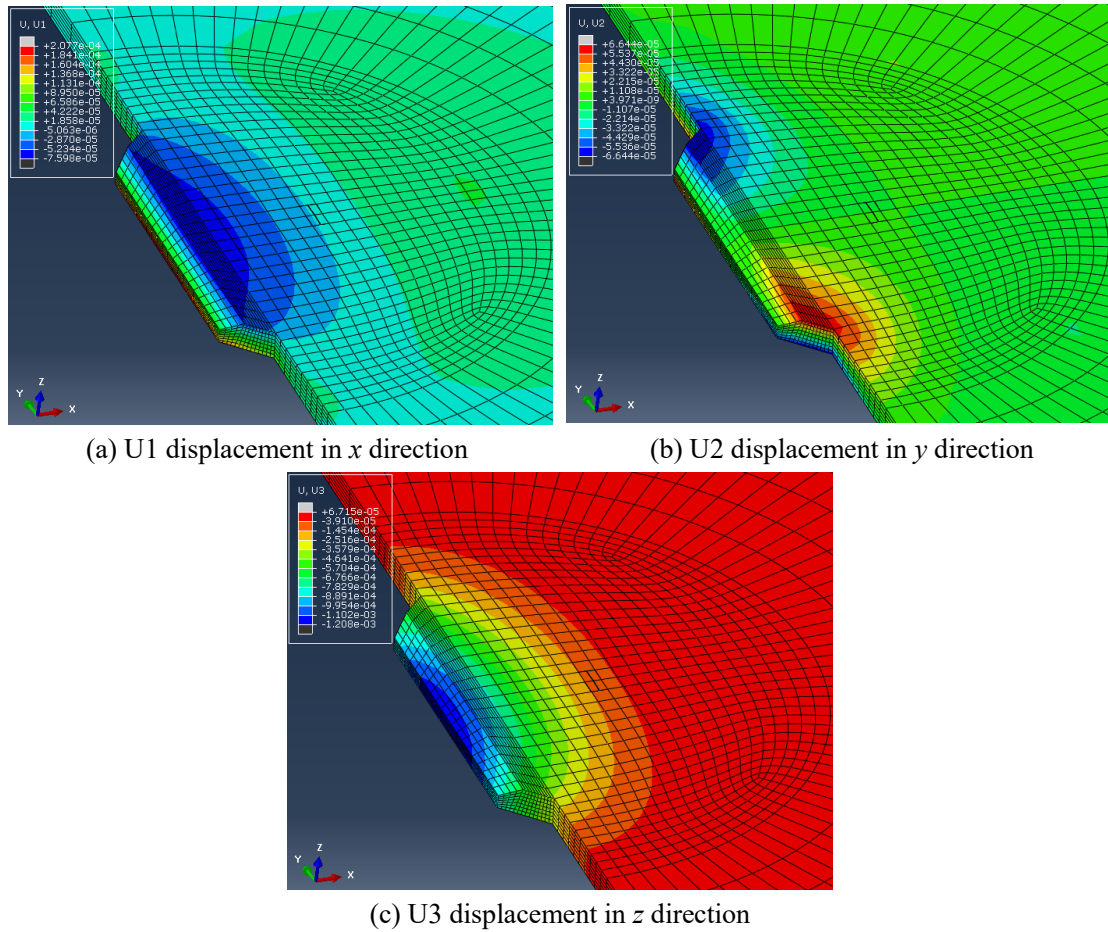


Figure 7. The deformation of level ice along  $x/y/z$  axis at  $t=7\text{ms}$ .

The U3 displacement at different time in Figure 8 shows the variation of level ice bending. The ice in the contact area has the largest displacement downward, while the ice around  $x=3\text{m}$  bulges upward and gradually decreases to 0 farther away from the contact area. This should be caused by the springs at the bottom of the level ice.

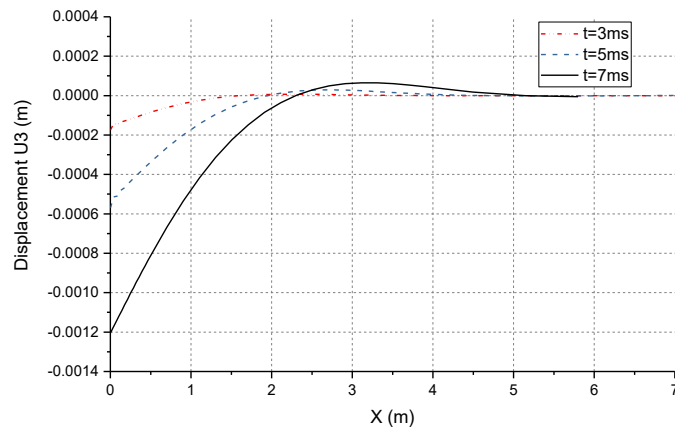


Figure 8. The vertical displacement of the level ice of the center line ( $\beta=50^\circ$ ,  $v=2\text{m/s}$ )

#### 4.1.3 Ice stress distribution

The bending crack initiates from the top surface of the level ice, and the stress distribution of the top surface may help to explain the mechanism of bending crack. Figure 9-10 display the ice stress components S11 in  $x$  direction, S22 in  $y$  direction, maximum principal stress and hydrostatic stress of the top surface at the crack initiation time ( $t=7\text{ms}$ ). It should be noted that the positive value

represents compressive state for hydrostatic stress, and tensile state for other stresses. Table 6 summarizes the extreme values and the corresponding locations of different stresses of the whole ice.

Table 6. The extreme values of stresses and the corresponding locations

stress	$S_{11}$	$S_{22}$	Maximum principal stress	Hydrostatic stress
Maximum tensile value(MPa)	0.4112	0.2614	0.4686	0.2087
Location (m)	Top midline $x=1.51$	Bottom edge midpoint	Top wedge corner	Top midline $x=1.71$
Maximum compressive value(MPa)	0.5594	0.3217	0.6260	0.2631
Location (m)	Bottom midline $x=1.51$	Central contact area	Bottom wedge corner	Bottom midline $x=1.71$

At the top surface of the level ice,  $S_{11}$  stress is distributed as the “growth ring” pattern, which is quite similar with the distribution of  $f$ -value in Figure 4. The stress value is high around the initiation crack and getting lower at the outer positions. The maximum  $S_{11}$  is at  $x=1.51$ m of top surface midline, and the initial crack is at  $x=1.8$ m. The  $S_{11}$  stress of contact area is tensile stress. The distribution of  $S_{22}$  stress shows a “belt” pattern. The  $S_{22}$  stresses around the initial crack and both wedge corners are higher than the stresses of other places and are also in tensile state. While around the contact area,  $S_{22}$  is compressive stress and the maximum  $S_{22}$  compressive stress is located at here.

The maximum principal stresses at the wedge corners and initial crack area are higher than other places and are all tensile stress. At the crack initiation time, the maximum principal stresses occur at one corner of the ice wedge. Throughout the dynamic analysis process, the maximum value of the maximum principal stress does not always appear here, but alternately at the corners as well as at the top surface midline. The maximum principal stress indicates that both corners and the midline are failure hazard zones.

For the hydrostatic stress, negative value represents tensile state. Figure 10 (right) marked its minimum value and location, which represents the corresponding node is at most tensile state. The minimum value of hydrostatic stress is 0.2087MPa and located at  $x=1.71$ m of top surface midline. Comparing it with the distribution of  $f$ -value at crack initiation time ( $t=7$ ms) in Figure 4, it could be found that the node with minimum hydrostatic stress is subordinate to the element with initial crack, and is the same node with the maximum  $f$ -value.

The above analysis shows that level ice is bent when impacted by the rigid plate. And some area of the top surface of ice is stretching under the impaction, this tensile state is closely related to the crack initiation. In this simulated case, the minimum hydrostatic stress is very close to the node of initial crack, indicating that comparing with other stresses, the hydrostatic stress may be more associated with the bending crack initiation.

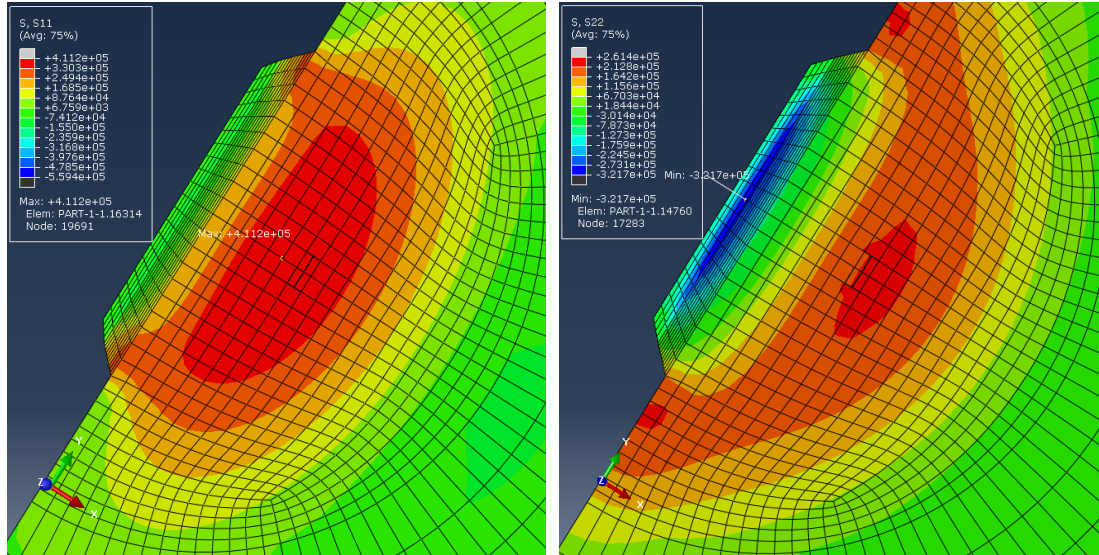


Figure 9. The stress in x direction and y direction of top surface of level ice

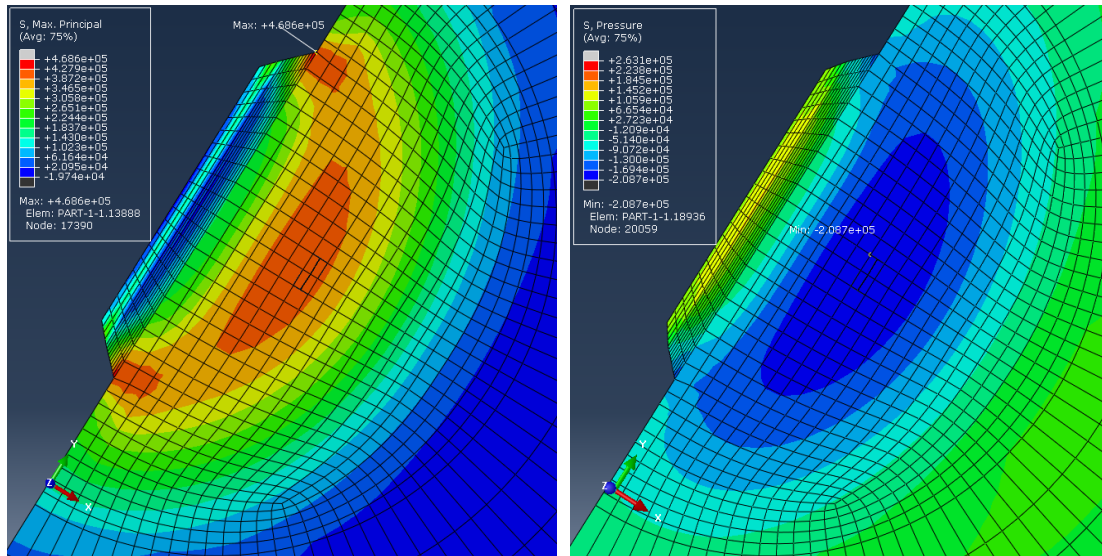


Figure 10. The maximum principal stress (left) and hydrostatic stress (right) of top surface of level ice

## 4.2 Splitting fracture

### 4.2.1 Splitting fracture initiation and propagation

In the cases of  $\beta=30^\circ$ ,  $v=1.2\text{m/s}$ , a splitting crack is obtained. The splitting crack emerges at the bottom surface of the level ice. Figure 11 shows the development of  $f$ -value at the bottom surface of the level ice, as well as the initiation and propagation of the splitting crack.

Along with the ice-structure interaction, the level ice deforms, and  $f$ -value develops. Compared to other area, the area of bottom surface closing to the free edge always maintained higher  $f$ -values. The maximum  $f$ -value appears here for most of the time except for  $t=10\text{ms}$  when the maximum  $f$ -value moves to the top surface. And after that, it moves back to the bottom edge area. At  $t=15\text{ms}$ ,  $f$ -value reaches 1 and the crack initiates in the element beside the bottom surface midline. The numerical result shows that  $f=1$  node belongs to the crack initiation element.

The initial crack is parallel to  $x$  axis as shown in Figure 11. Then it propagates along  $x$  axis, reaching the free edge in the negative direction, and extending in the positive direction, then a splitting crack gradually forms. It has been defined that the crack propagates in the direction vertical

to the maximum principal stress, then it could be speculated that the maximum principal stress is perpendicular to the  $x$  axis in the crack propagation process.

In the simulated process, the  $f$ -value of other area never comes to 1, and no other cracks emerge. Figure 12 shows the  $f$ -value distribution of the top surface at  $t=15\text{ms}$ , indicating that the top surface also maintains high  $f$ -value at the splitting crack initiation time. But after the splitting crack emerges, the top surface stresses are relieved, and the  $f$ -value here does not reach 1. The splitting crack continues to propagate, until the computation no longer converges, and the final ice load can't be obtained.

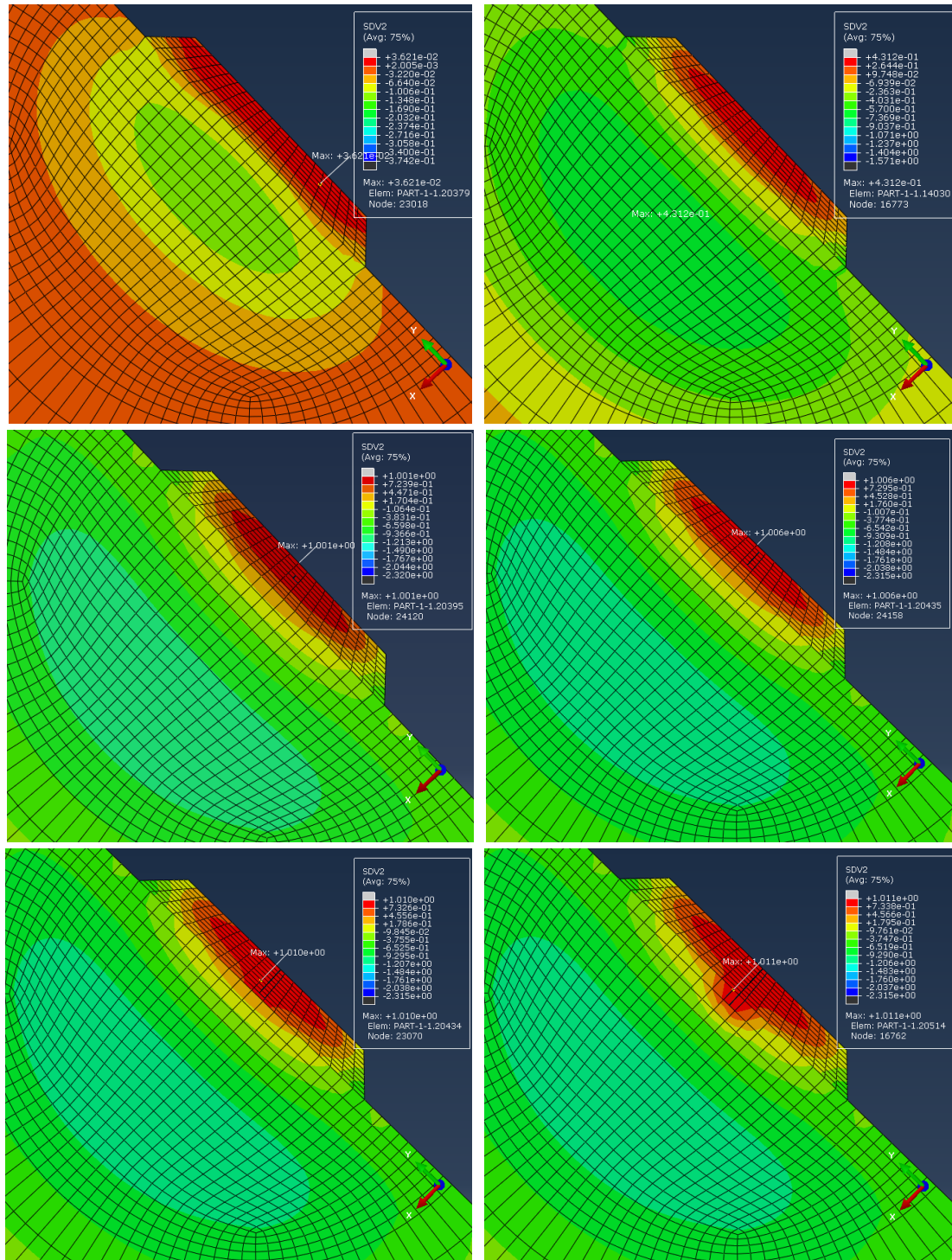


Figure 11. Distribution of crack initiation function  $f$  at bottom surface of the level ice. Time  $t=3\text{ms}, 10\text{ms}, 15\text{ms}, 16\text{ms}, 17.9\text{ms}, 20.9\text{ms}$  in the case of  $\beta=30^\circ, v=1.2\text{m/s}$ .

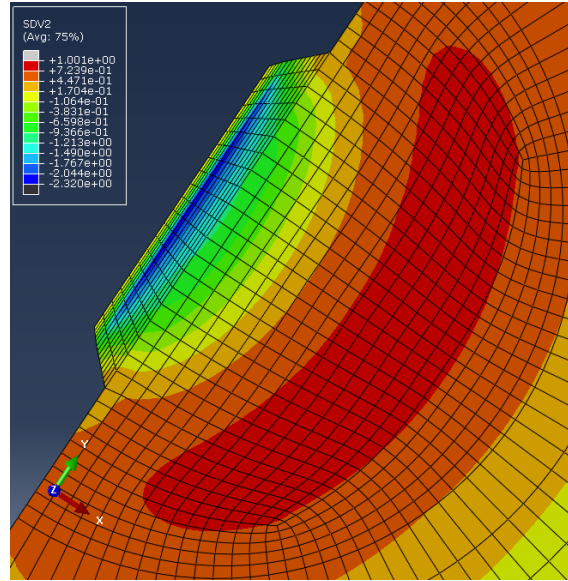


Figure 12. Distribution of crack initiation function  $f$  at top surface of the level ice at  $t=15\text{ms}$

#### 4.2.2 Ice stress distribution

The above analysis has found that the splitting crack initiates from the bottom surface closing to the free edge. This section analyzes the S11 stress, S22 stress, maximum principal stress and hydrostatic stress distribution of the level ice's bottom surface at the crack initiation time ( $t=15\text{s}$ ), which are shown in Figure 13-14. The extreme value of the whole ice of different stresses are marked in the figures and are summarized with their locations in Table 7. And positive value still represents compressive state for hydrostatic stress, tensile state for other stresses.

The S11 stress of the middle area of the bottom surface of level ice is in compressive state, and the S22 stress in free edge of the bottom surface is in tensile state. This result shows that in the process of level ice deforming, the bottom surface is compressed along  $x$  direction. While in  $y$  direction, the area closing to free edge of bottom surface is stretched, then generates tensile stress in this direction.

For the maximum principal stress and hydrostatic stress, the area near the free edge of the bottom surface is in high tensile states, and the maximum tensile stresses also occur here. Figure 15 shows the hydrostatic stress of the bottom surface midline of the level ice. As  $x$  increases, the hydrostatic stress first decreases a bit, then increases from negative to positive values. After reaches the curve peak, it decreases again and gradually converges to 0. The minimum hydrostatic stress does not occur at  $x=0$ , but at  $x=0.2\text{m}$ . The crack initiates at the fourth element along  $x$  direction. And the numerical simulation shows that the node with the minimum hydrostatic stress belongs to the element where the crack initiates.

The node with the maximum value of maximum principal stress and the node with minimum hydrostatic stress of level ice are very close, both near the initial crack, indicating that the initiation of the crack at the bottom of level ice is closely related to the tensile state in this area. Besides, the extreme values of maximum principal stress and S22 stress are similar, are  $0.5158\text{MPa}$  and  $0.5155\text{MPa}$  respectively, indicating that the stress component S22 in  $y$  direction is the main reason for the strong tensile state in this area. This further indicates that the splitting crack's initiation is mainly caused by the stretching in  $y$  direction.

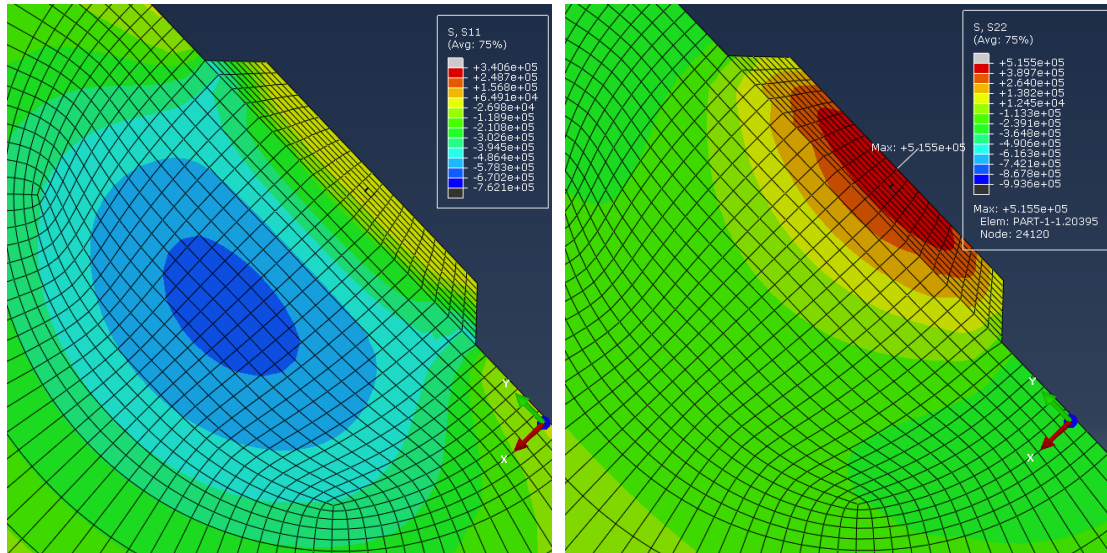


Figure 13. The stress in x direction (S11, left) and y direction (S22, right) of the bottom surface of level ice

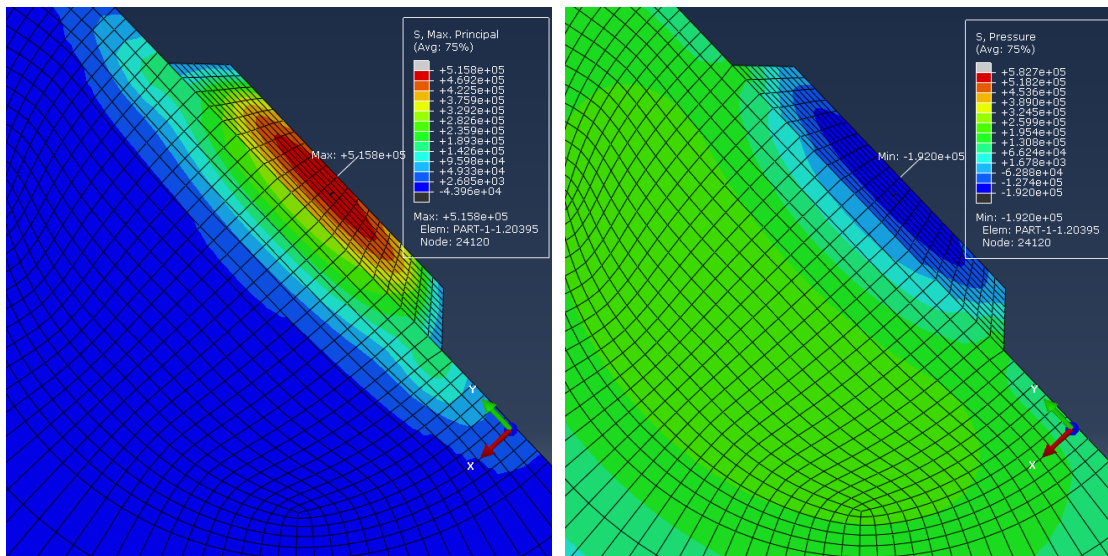


Figure 14. The maximum principal stress (left) and hydrostatic stress (right) of the bottom surface of level ice

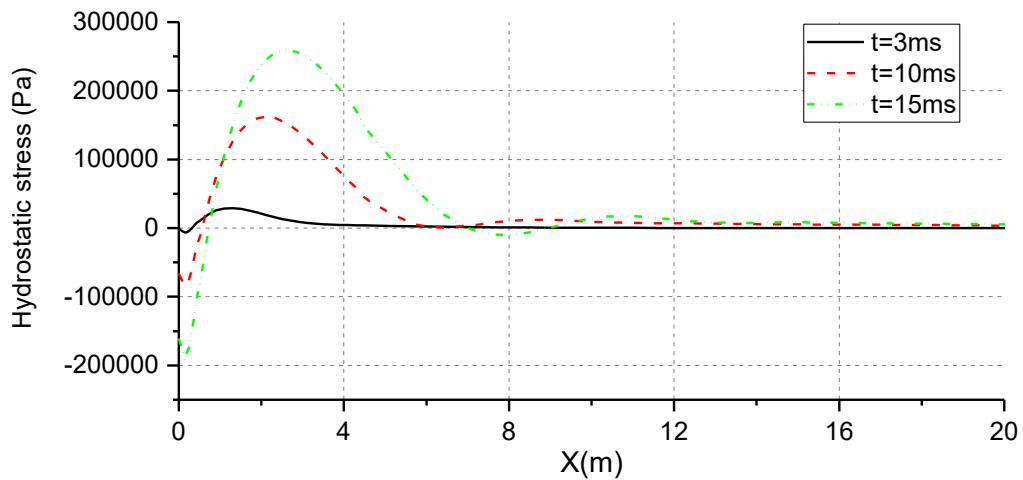


Figure 15. Hydrostatic stress of midline of bottom surface of level ice

Table 7. The extreme value of different stresses and the corresponding location

stress	$S_{11}$	$S_{22}$	Maximum principal stress	Hydrostatic stress
Maximum tensile value(MPa)	0.3406	0.5155	0.5158	0.1920
Location (m)	Top midline $x=2.5$	Bottom midline $x=0.2$	Bottom midline $x=0.2$	Bottom midline $x=0.2$
Maximum compressive value(MPa)	0.7621	0.9936	0.04396	0.5027
Location (m)	Top contact area	Top contact area	Top contact area	Top contact area

Combining the analysis of bending process and splitting process, cracks may occur at the top surface midline and the bottom surface free edge area, corresponding to bending crack and splitting crack respectively, which are both related to the local tensile state of the level ice. In the process of structure-ice interaction, the stresses of both areas are developing and competing with each other. In the  $\beta=30^\circ$ ,  $v=1.2\text{m/s}$  case, the tensile stress of the bottom surface develops faster than that of the top surface, then splitting crack initiates first. The difference of this case with the bending crack case of section 4.1 is the impact velocity and inclination angle of the structure. In the next section, the results of more cases will be compared.

#### 4.3 The influence of velocity and inclination angle on ice fracture

##### 4.3.1 Fracture mode and ice load

In all the simulated cases, bending crack initiates at the top surface midline, and splitting crack initiate at the bottom surface closing to the contact edge. In the 3 cases of inclination of  $50^\circ$ , only bending crack appears. In the 3 cases of inclination angle of  $30^\circ$ , only bending crack appears when the impact velocity is  $3\text{m/s}$ , bending crack and splitting crack appear at the same time when the velocity is  $2\text{m/s}$ , and only splitting crack appears when the velocity is  $1.2\text{m/s}$ .

The simulation and test results of ice load and fracture size of the 5 cases where bending crack emerges are compared in Figure 16. At the same inclination angle, the simulated ice load increases as the impact velocity increases, and this trend is the same with the test results. In the field test, the ice load's increasing trend with velocity of  $50^\circ$  cases is more obvious than that of  $30^\circ$  cases, and the ice load of the latter cases are more discrete. At the same collision velocity, the inclination angle of the structure has a significant influence on the ice load. As the inclination angle increases, the bending ice load decreases. The proportion of the vertical component of the contact force becomes larger, and the total force needed to bend the level ice decreases. The simulated and test crack sizes correspond well. In the field test, the crack size  $d$  did not show obvious tend, while the simulated crack size  $d$  decreases as the impact velocity or the inclination angle increases. The difference of the simulated and test results may be because the lack of hydrodynamic simulation and the randomness of the sea ice.

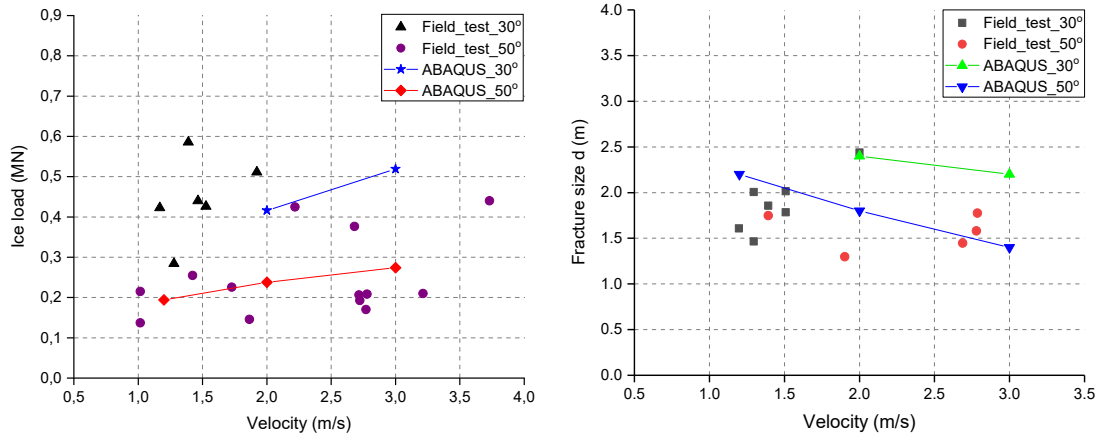


Figure 16. Comparison of the ice load (left) and bending crack size  $d$  (right) of field test and numerical simulation at different velocity and inclination angle.

The simulated result shows that the fracture mode of the level ice is correlated with the collision velocity and inclination angle of the structure. Table 8 summarized the  $f$ -values of the level ice in 6 cases at the crack initiation time. In the cases of inclination angle of  $50^\circ$ , the maximum  $f$ -value of bottom surface is lower than  $f$ -value of top surface, thus the bending crack initiates from the top surface in the 3 cases. And as the impact velocity increases, the difference of  $f$ -value of top surface and bottom surface increases, and the level ice is easier to have bending crack. In the cases of inclination angle of  $30^\circ$ , the difference of the two  $f$ -values is smaller compared to  $50^\circ$  cases. As the impact velocity increases, the top surface  $f$ -value gradually exceeds the bottom surface  $f$ -value. For the 2m/s case, the top and bottom  $f$ -values equal to 1 at the same time. Correspondingly, the crack mode of the level ice changes from splitting crack to bending crack as the velocity increases, and splitting crack and bending crack appear at the same time in 2m/s case. It can be concluded that level ice is easier to be bent than to be split as the impact velocity improving or the inclination angle is higher. And after the appearance of one type of crack, another type of crack's initiation and propagation may be suppressed.

The results show that in the level ice-structure interaction, bending crack is easier to emerge as the inclination angle increases, and splitting crack is easier to emerge as the inclination angle decreases. Compared to splitting crack, bending crack of level ice corresponds to smaller ice load. The larger inclination angle results in smaller ice load. As the impact velocity increases, bending crack is easier to emerge, and as the impact velocity decreases, splitting crack is easier to initiate.

Table 8. Maximum crack initiation function  $f$  along the midline of upper surface and lower surface.

Case	Top surface $f$ -value		Bottom surface $f$ -value	
	Value	Location $x$ (m)	Value	Location $x$ (m)
$\beta=30^\circ, v=1.2\text{m/s}$	0.814	2.91	1.001	0.15
$\beta=30^\circ, v=2\text{m/s}$	1.029	2.31	1.005	0.15
$\beta=30^\circ, v=3\text{m/s}$	1.005	2.11	0.945	0.15
$\beta=50^\circ, v=1.2\text{m/s}$	1.005	2.11	0.744	0
$\beta=50^\circ, v=2\text{m/s}$	1.004	1.71	0.439	0
$\beta=50^\circ, v=3\text{m/s}$	1.005	1.307	0.262	0

#### 4.3.2 Deformation and stresses of the level ice

This part analyzes the influence of impact velocity and inclination on level ice deformation and

stress. Figure 17 to Figure 20 illustrate separately the vertical deformation  $U_3$ , maximum principal stress, hydrostatic stress and  $f$ -value on the top surface midline of the level ice under different impact velocities and inclination angles. Table 9 summarizes the extreme value of hydrostatic stress and maximum principal stress of the whole level ice in different cases.

Figure 17 compares the vertical deformation  $U_3$  of ice midline at the crack initiation time under different impact velocities and inclination angles. In the same inclination angle, the ice displacement  $U_3$  at  $x=0$  gets smaller as the impact velocity is higher. For example, the vertical displacement is  $-0.89\text{mm}$  at impact velocity of  $3\text{m/s}$  and inclination angle of  $50^\circ$  and is  $-2.09\text{mm}$  at impact velocity of  $1.2\text{m/s}$ . The deforming range in  $x$  direction is also getting smaller at higher impact velocity. However, in the case that inclination angle is  $30^\circ$  and impact velocity is  $1.2\text{m/s}$ , although the  $U_3$  deformation is still in accordance with the above law, its  $U_3$  curves is similar with the  $U_3$  curve of  $2\text{m/s}$ . That's because in the case of  $1.2\text{m/s}$ , the crack initiates at the bottom surface of level ice, thus the ice deformation of top surface midline is not representative. In the same impact velocity, the ice displacement  $U_3$  at  $x=0$  and the deforming range are both getting smaller as the impact inclination is larger. This indicates that for higher impact velocity and larger impact inclination, the bending deformation  $U_3$  becomes smaller and more concentrated in a smaller range.

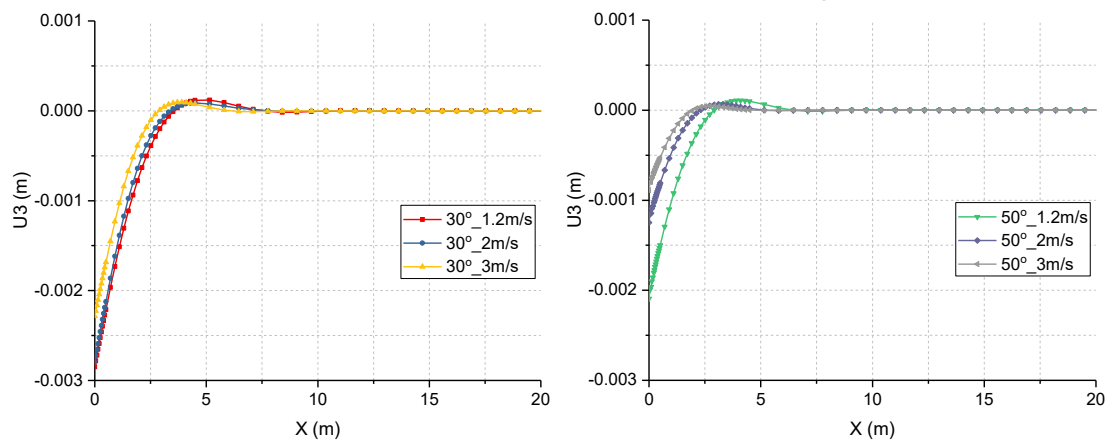


Figure 17. Vertical displacement  $U_3$  of level ice along  $x$  axis under different impact velocity and inclination angle

The distribution of the maximum principal stress at the top surface midline of the level ice is illustrated in Figure 18. When the inclination angle is  $50^\circ$ , the distribution of maximum principal stress is more concentrated as the impact velocity is higher. This corresponds well with the distribution of bending deformation. The peak of the maximum principal stress is closer to the contact area ( $x=0$ ), and the peak value is lower as the impact velocity is higher. When the inclination angle is  $30^\circ$ , the results of velocity of  $2\text{m/s}$  and  $3\text{m/s}$  are consistent with the above rule. While for the velocity of  $1.2\text{m/s}$ , the peak value of maximum principal stress is instead the smallest, and the stress curve is flatter compared to the other two curves. Although the  $U_3$  deformation curves for  $1.2\text{m/s}$  and  $2\text{m/s}$  are similar, their stress curves differ a lot. For the same impact velocity and different inclination angles, the peak values of the maximum principal stress are similar, and the peaks seem to be closer to the contact area when the inclination angle is larger.

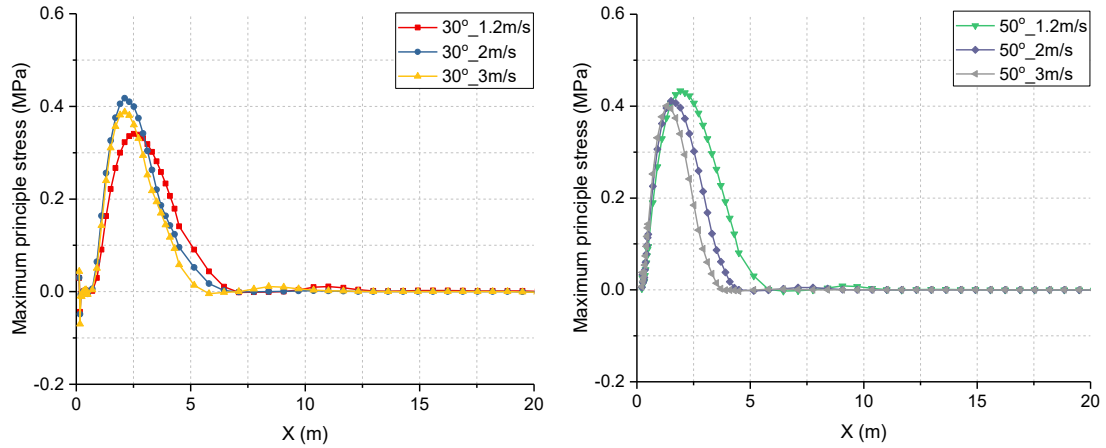


Figure 18. Maximum principal stress of level ice on the top along  $x$  axis under different impact velocity and inclination angle

In the numerical simulation, the peak value of maximum principal stress of the whole ice does not appear at the top surface midline, as summarized in Table 9. For the cases of  $30^\circ$  inclination angle, the peak value of maximum principal stress of the whole ice is at the bottom surface closing to the contact edge. And the splitting crack initiates here in the case of  $\beta=30^\circ$ ,  $v=1.2\text{m/s}$ , as shown in Figure 14 (left). For the cases of bending crack case, the peak value of maximum principal stress of the whole ice is at wedge corner of the top surface, as shown in Figure 10 (left). In most cases, the peak maximum principal stress and the location of the initial crack do not appear at the same place.

Figure 19 and 20 shows the hydrostatic stress and  $f$ -value of top surface midline at crack initiation time separately. Besides of  $\beta=30^\circ$ ,  $v=1.2\text{m/s}$ , the minimum hydrostatic stresses of different impact velocities and inclination angles are at the top surface midline and agree well with the crack initiation locations. The minimum hydrostatic values are very close, around  $-0.21\text{MPa}$ , as illustrated in Figure 19 and Table 9. For the case of  $\beta=30^\circ$ ,  $v=1.2\text{m/s}$ , the minimum hydrostatic stress of the top surface midline is  $-0.17\text{MPa}$ , it's lower than the other cases. In this case, the crack appears at the bottom surface, and the corresponding hydrostatic stress is also at this area, the value is  $-0.192\text{MPa}$ . It can be summarized that in all the cases, the simulated initial crack's location always corresponds with the minimum hydrostatic stress of the level ice. Table 9 illustrated the extreme values of maximum principal stress and hydrostatic stress and their locations.

The hydrostatic stress becomes more concentrated as the impact velocity getting higher, and as the inclination angle getting larger. For the maximum hydrostatic stress representing the compressive state, its value under  $30^\circ$  is much higher than that under  $50^\circ$ . It confirms that in the contact area, the compressive stress of level ice caused by a structure of  $30^\circ$  inclination angle is significantly higher than the stress caused by a structure of  $50^\circ$ .

If we compare the hydrostatic stress and  $f$ -value curves, it could be found that their shapes are quite similar, just in opposite direction. The locations of the maximum  $f$ -value and minimum hydrostatic stress correspond well, and the curves' variation with impact velocity and inclination angle are also the same.

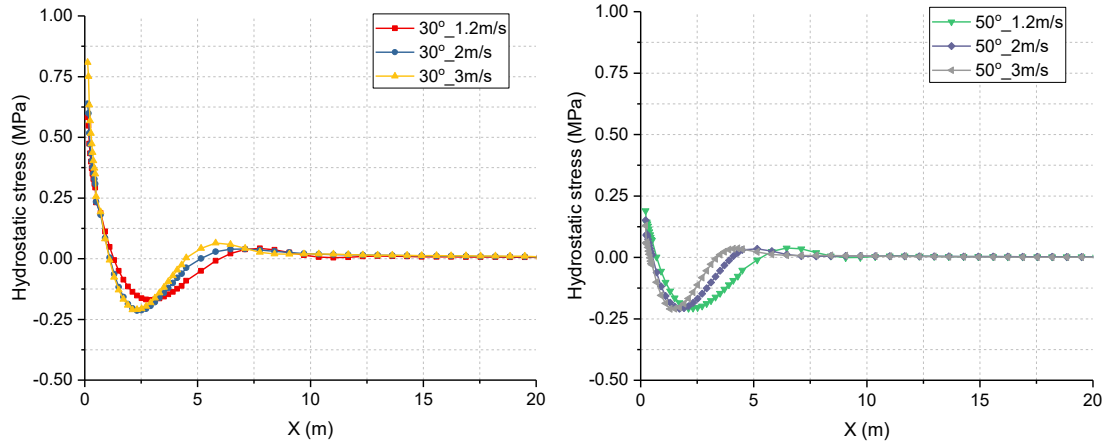


Figure 19. Hydrostatic stress of level ice on the top surface along  $x$  axis under different impact velocity and inclination angle

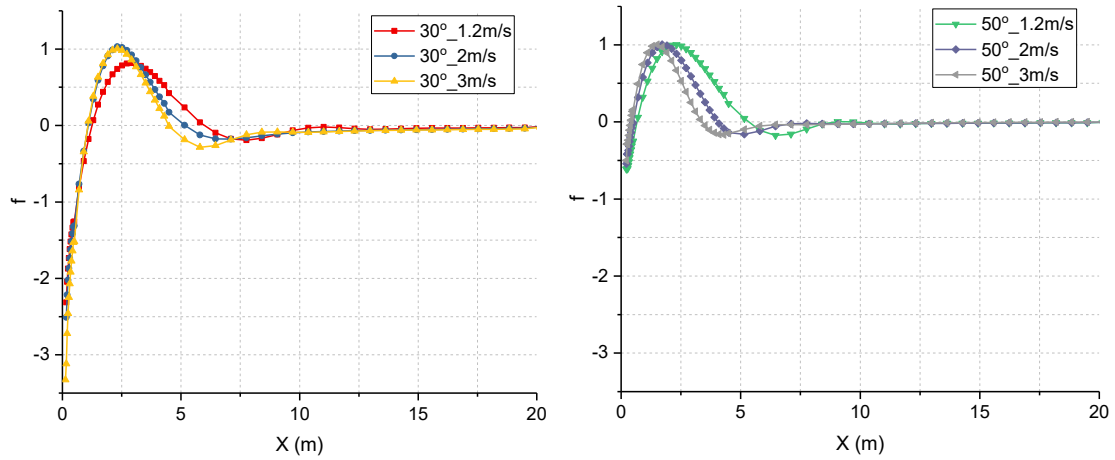


Figure 20.  $F$ -value of level ice on the top surface along  $x$  axis under different impact velocity and inclination angle

Table 9. Distribution of the extreme value of hydrostatic stress and maximum principal stress in different cases

Case	Initial crack's locaton	Hydrostatic stress		Maximum principal stress	
		Minimum value (MPa)	Location	Maximum value (MPa)	Location
$\beta=30^\circ, v=1.2\text{m/s}$	Bottom midline	-0.192	Bottom midline	0.5158	Bottom midline
$\beta=30^\circ, v=2\text{m/s}$	Top midline	-0.2143	Top midline	0.5196	Bottom midline
$\beta=30^\circ, v=3\text{m/s}$	Top midline	-0.2101	Top midline	0.4801	Bottom midline
$\beta=50^\circ, v=1.2\text{m/s}$	Top midline	-0.2069	Top midline	0.5412	Top wedge corner
$\beta=50^\circ, v=2\text{m/s}$	Top midline	-0.2087	Top midline	0.4686	Top wedge corner
$\beta=50^\circ, v=3\text{m/s}$	Top midline	-0.2095	Top midline	0.4051	Top wedge corner

Note: negative value of hydrostatic stress represents tensile state; positive value of maximum

principal stress represents tensile state.

Improving the impact velocity and inclination angle will lead to smaller ice deformation at crack initiation time, and smaller crack size  $d$ . The peak value of the maximum principal stress of top surface midline will reduce as the velocity increases, and the minimum hydrostatic stresses are similar in different velocities and inclinations. Besides, the peak value of the maximum principal stress of top surface midline is not the extreme value of the whole ice. The extreme value of maximum principal stress of the whole ice appears at the bottom edge and top surface wedge corner. The minimum hydrostatic stress of top surface midline is the extreme value of the whole ice, and its location corresponds well with the crack initiation area (f-value equals 1). Compared to maximum principal stress, the simulated minimum hydrostatic stress corresponds better with the crack initiation criterion. That means if the minimum hydrostatic stress is used as the crack initiation criterion, the predicted initial crack would be the same with Tsai-Wu criterion.

#### 4.3.3 Time information of ice deformation and stress

The deforming process of level ice under different impact velocities is shown in Figure 21. In order to compare the deforming process of level ice, the deformation curves at the same time after ice-plate contact in different cases are marked with the same color and symbol. For example, at  $t=3\text{ms}$ , the  $U_3$  displacement at the contact area of case  $50^\circ\_3\text{m/s}$  is larger than that of the case  $50^\circ\_1.2\text{m/s}$ . An important factor contributing to this result is obviously the faster movement of the rigid plate and the collision force growth. After the structure contacts with level ice, deformation will propagate from the contact point to surrounding before fracture occurs. A lower forward speed means that the deformation will have more time to travel farther before fracture occurs. In case  $50^\circ\_1.2\text{m/s}$ , the deformation of level ice at  $t=11.2\text{ms}$ , when the crack initiates, is larger and in a wider range compared to the cases with higher velocity. And this will result in a larger fracture size eventually.

Through the above analysis, it's found the hydrostatic stress is more appropriate for judging the crack initiation compared to other stresses in this work. Then the hydrostatic stress variation is also illustrated here to correspond to the deformation diagrams. It could be found that the hydrostatic stress at higher impact velocity increases faster than that at a slower velocity. Although the position of the maximum hydrostatic stress at the same time is a bit farther from the contact point for higher impact velocity, it increases faster and reached the failure point earlier.

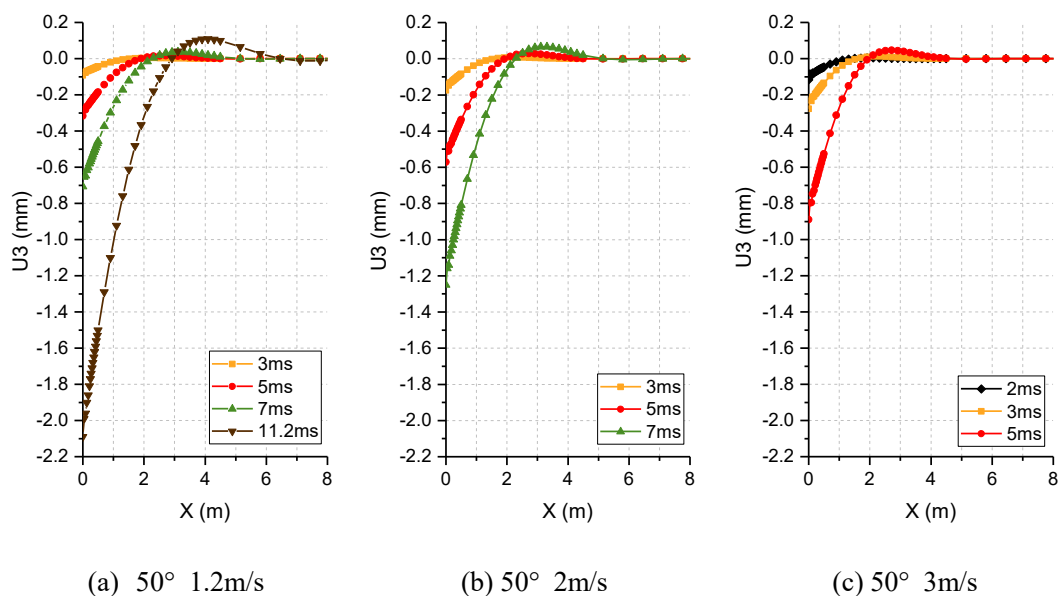


Figure 21. Variation of vertical displacement U3 in time under different impact velocity

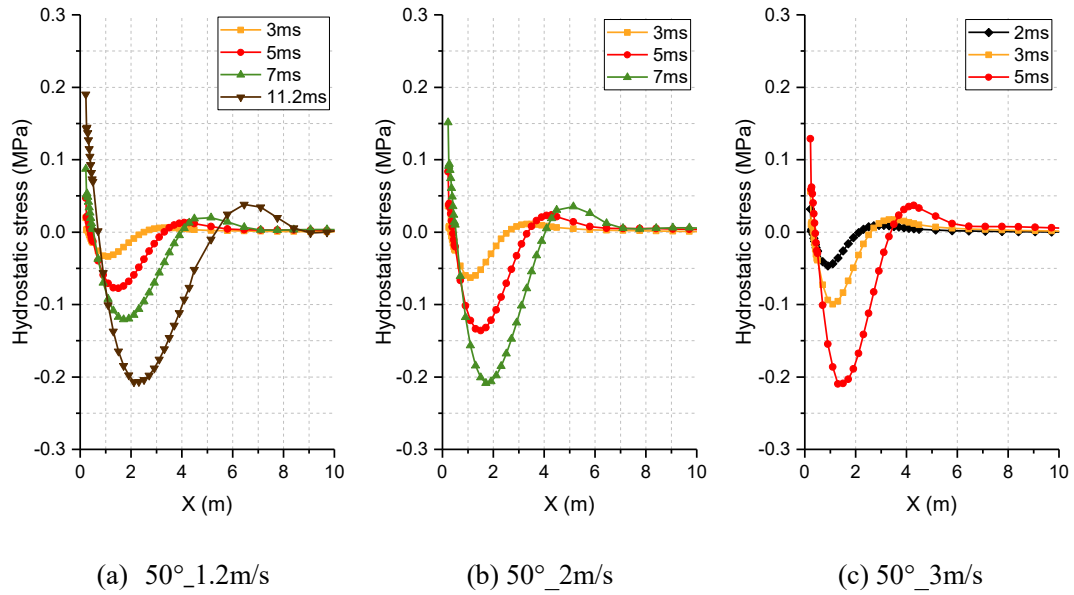


Figure 22. Variation of hydrostatic stress in time under different impact velocity

## 5. Conclusion

In this paper, the fracture mechanism of level ice is investigated by simulation using extended finite element method and cohesive model. A collision scenario between level ice and a rigid plate is modeled, and the transversely isotropic elastic material model and crack initial criterion are adopted for the simulation.

The numerical results show two fracture modes of the level ice, bending fracture and splitting fracture, emerge in level ice. It is found that the bending fracture initiates from the midline of the upper surface of the ice and expands toward the free edge, and the splitting crack initiates at the midline of the bottom surface of the level ice closing to the free edge and expands along the radial direction. The simulated results of bending crack are in good agreement with the experimental results. Splitting failure is not found in the experimental record, and the reason for this difference between the numerical and experimental results may be that hydrodynamics and the temperature gradient between the upper and lower surfaces of the level ice are not accounted for in the numerical simulations. It should be noticed that the findings do not yet have general validity.

The distribution of deformation and stresses of level ice are analyzed in this work, including stress components S11 and S22, maximum principal stress as well as hydrostatic stress. It is found that the initial crack is closely related to the local tensile failure for both fracture modes. The rigid plate makes the level ice generate downward bending deformation and in-plane compressive deformation, leading to tensile stress in the central area of the top surface and in the free edge area of the bottom surface of the level ice, then the initial crack appears in the corresponding area. The stress distribution shows that the location of the minimum hydrostatic stress is almost identical to the location of the initial crack, indicating that comparing to other stresses, the hydrostatic stress may be more associated with the crack initiation.

Finally, the effects of collision velocity and inclination of the rigid plate on the ice fracture mode, ice load and bending crack size are analyzed. Velocity and inclination angle affect the fracture mode through changing the stress distribution of level ice. The simulated results show that the fracture mode is determined mainly by the development status of the tensile state of the top surface

and tensile state of the edge area of the bottom surface of the level ice. The increase of collision velocity and inclination angle between the rigid plate and the vertical direction will make the tensile stress of the top surface develop faster, thus the level ice tends to be broken by bending fracture; conversely, the level ice tends to split. Besides, the increase of collision velocity leads to higher ice load, and makes the bending crack closer to the contact edge, which result in smaller broken ice. Along with the increase of inclination angle, the bending ice load and the size of the broken ice get decreased.

## Reference

- ABAQUS 2019 analysis user's guide. Dassault Systemes Simulia Corp. 2019.
- Dempsey, J. P., Cole, D. M., & Wang, S. (2018). Tensile fracture of a single crack in first-year sea ice. *Philosophical Transactions of the Royal Society A: Mathematical, Physical and Engineering Sciences*, 376(2129), 20170346.
- Ehlers, S., & Kujala, P. (2014). Optimization-based material parameter identification for the numerical simulation of sea ice in four-point bending. *Proceedings of the Institution of Mechanical Engineers, Part M: Journal of Engineering for the Maritime Environment*, 228(1), 70-80.
- Gürtner, A. (2009). *Experimental and Numerical Investigations of Ice-Structure Interaction* (Ph.D. thesis). Norwegian University of Science and Technology.
- Jeon, S., & Kim, Y. (2021). Numerical simulation of level ice–structure interaction using damage-based erosion model. *Ocean Engineering*, 220, 108485.
- Keinonen, A. (1996). *Icebreaker characteristics synthesis*.
- Kellner, L., Lu, W., Ehlers, S., & Høyland, K. V. (2021). Study on the cohesive edge crack in a square plate with the cohesive element method. *International Journal of Fracture*, 231(1), 21-41.
- Kerr, A. D. (1976). The bearing capacity of floating ice plates subjected to static or quasi-static loads. *Journal of glaciology*, 17(76), 229-268.
- Li, F., Kõrgesaar, M., Kujala, P., & Goerlandt, F. (2020). Finite element based meta-modeling of ship-ice interaction at shoulder and midship areas for ship performance simulation. *Marine Structures*, 71, 102736.
- Lilja, V. P., Polojärvi, A., Tuhkuri, J., & Paavilainen, J. (2019). A free, square, point-loaded ice sheet: A finite element-discrete element approach. *Marine Structures*, 68, 102644.
- Lindquist, A. (1989). Straightforward method for calculation of ice resistance of ships. *POAC'89*.
- Liu, L., & Ji, S. (2021). Dilated-polyhedron-based DEM analysis of the ice resistance on ship hulls in escort operations in level ice. *Marine Structures*, 80, 103092.
- Liu, Z., Amdahl, J., & Løset, S. (2011). Plasticity based material modelling of ice and its application to ship-iceberg impacts. *Cold regions science and technology*, 65(3), 326-334.
- Lu, W., Lubbad, R., Løset, S., & Høyland, K. V. (2012, June). Cohesive zone method based simulations of ice wedge bending: a comparative study of element erosion, CEM, DEM and XFEM. In *The 21st IAHR International Symposium on Ice* (pp. 920-938).
- Lu, W., Lubbad, R., & Løset, S. (2014). Simulating ice-sloping structure interactions with the cohesive element method. *Journal of Offshore Mechanics and Arctic Engineering*, 136(3).
- Lu, W., Lubbad, R., & Løset, S. (2015). Out-of-plane failure of an ice floe: radial-crack-initiation-controlled fracture. *Cold regions science and technology*, 119, 183-203.
- Lu, W., Heyn, H. M., Lubbad, R., & Løset, S. (2017). Large scale simulations of floe-ice fractures and validation against full-scale data. In *24th International Conference on Port and Ocean Engineering under Arctic Conditions (POAC 2017)* Location: Busan, Korea, South.

Lu, W., Lubbad, R., Shestov, A., & Løset, S. (2018). Parallel channels' fracturing mechanism during ice management operations. Part I: theory. *Cold Regions Science and Technology*, 156, 102-116.

Ni, B. Y., Chen, Z. W., Zhong, K., Li, X. A., & Xue, Y. Z. (2020). Numerical simulation of a polar ship moving in level ice based on a one-way coupling method. *Journal of Marine Science and Engineering*, 8(9), 692.

Patil, A., Sand, B., Cwirzen, A., & Fransson, L. (2021). Numerical prediction of ice rubble field loads on the Norströmsgrund lighthouse using cohesive element formulation. *Ocean Engineering*, 223, 108638.

Riska, K., Wilhelmson, M., Englund, K., & Leiviskä, T. (1997). Performance of Merchant Vessels in the Baltic (Research report no 52). Winter Navigation Research Board.

Riska, K. (2010). Ship-ice interaction in ship design: theory and practice. *Encyclopedia of Life Support Systems (EOLSS)*: Paris, France.

Sazidy, M. S. (2015). Development of velocity dependent ice flexural failure model and application to safe speed methodology for polar ships (Doctoral dissertation, Memorial University of Newfoundland).

Su, B., Riska, K., & Moan, T. (2010). A numerical method for the prediction of ship performance in level ice. *Cold Regions Science and Technology*, 60(3), 177-188.

Wang, F., Zhou, L., Zou, Z. J., Song, M., Wang, Y., & Liu, Y. (2019). Study of continuous icebreaking process with cohesive element method. *Brodogradnja*, 70(3), 93-114.

Varsta, P. (1983). On the mechanics of ice load on ships in level ice in Baltic Sea.

Vazic, B., Oterkus, E., & Oterkus, S. (2019). Peridynamic approach for modelling ice-structure interactions. In *Trends in the Analysis and Design of Marine Structures: Proceedings of the 7th International Conference on Marine Structures (MARSTRUCT 2019, Dubrovnik, Croatia, 6-8 May 2019)* (p. 55). CRC Press.

Xu, Y., Hu, Z., Ringsberg, J. W., & Chen, G. (2019). Nonlinear viscoelastic-plastic material modelling for the behaviour of ice in ice-structure interactions. *Ocean Engineering*, 173, 284-297.

Xu, Y., Kujala, P., Hu, Z., Li, F., & Chen, G. (2020). Numerical simulation of level ice impact on landing craft bow considering the transverse isotropy of Baltic Sea ice based on XFEM. *Marine Structures*, 71, 102735.

Xue, Y., Liu, R., Liu, Y., Zeng, L., & Han, D. (2019). Numerical simulations of the ice load of a ship navigating in level ice using peridynamics. *Computer Modeling in Engineering*, 523-550.

Zhou L, Wang F, Diao, Ding, & Yu. (2019). Simulation of ice-propeller collision with cohesive element method. *Journal of Marine Science and Engineering*, 7(10), 349.